Journal of Cleaner Production 414 (2023) 137611

Contents lists available at ScienceDirect

Journal of Cleaner Production

journal homepage: www.elsevier.com/locate/jclepro

Solarization of the zeolite production: Calcination of kaolin as proof-of-concept

Pelin Pasabeyoglu [a,c,*], Gkiokchan Moumin [b], Lamark de Oliveira [b], Martin Roeb [b], Burcu Akata [a,c]

[a] Micro and Nanotechnology Programme, Middle East Technical University, 06800, Ankara, Turkey
[b] Institute of Future Fuels, German Aerospace Center (DLR), 51147, Cologne, Germany
[c] Central Laboratory, Middle East Technical University, 06800, Ankara, Turkey

ARTICLE INFO

Handling Editor: Panos Seferlis

Keywords:
Solar calcination
Concentrated solar energy
Kaolin
Metakaolin
Zeolite 4A
Zeolite 13X

ABSTRACT

The current production of zeolites from natural sources requires high temperatures to achieve a phase change in the feedstock materials. Thermal processes such as calcination are energy-consuming and industry relies on fossil fuels to generate the necessary heat, which is neither sustainable nor environmental. This study presents for the first time the treatment of aluminosilicate clay kaolin in a solar reactor to produce metakaolins that are eligible as precursors for zeolite synthesis. Kaolin was loaded in a rotary kiln and a solar simulator was used for calcination at temperatures of 700–1000 °C for 2 h. After the solar calcination process, solar-produced metakaolins were used to synthesize zeolite 4 A and zeolite 13X by hydrothermal route. The kaolin, metakaolin, and product samples obtained were analyzed by XRD, XRF, FTIR, and FE-SEM. Results show that solar-calcined kaolin was as good and efficient as the conventionally calcined one in terms of supplying the metakaolin for zeolite synthesis. Often disregarded by researchers, high-temperature calcination of the kaolin was proved to be an alternative way for the synthesis of zeolite 13X without using an extra silica source, which was achieved for the first time. The overall results suggest that solar calcination is a good alternative to mass produce meta forms of the minerals to be used in the synthesis of value-added products such as zeolites.

1. Introduction

Kaolin is an essential industrial clay mineral known for its availability, low cost, and eco-friendliness making it one of the most thoroughly researched raw resources. Kaolinite ($Al_2Si_2O_5(OH)_4$) is the major phase in kaolin and is a 1:1 phyllosilicate that is composed of a silica layer bonded to the aluminum oxide/hydroxide layers with inner-surface and hydroxyl groups (Cheng et al., 2019). These hydroxyl groups are separated from the kaolinite crystal at high temperatures, resulting in substantial structural changes. During kaolinite calcination, four major thermally induced processes occur at different temperature ranges. These are dehydroxylation of kaolinite to metakaolinite (450–700 °C), formation of Al–Si spinel phase and amorphous silica from metakaolinite (925–1050 °C), formation of mullite (≥1050 °C), and crystallization of cristobalite from amorphous silica (≥1200 °C) (Ptáček et al., 2010; Sperinck et al., 2011). Other impurities, such as muscovite and quartz can also exist in kaolin, which is known to affect the decomposition behavior of kaolinite (Bergaya et al., 2006; Zhou et al., 2013).

The transformation of kaolin into metakaolin and the formation of new phases at different calcination temperatures have been extensively studied (Castelein et al., 2001; Lecomte et al., 2007; Zhou et al., 2013; Irfan Khan et al., 2017; Khaled et al., 2023). As demonstrated in Eq. (1), the process that results in metakaolin produces H_2O rather than CO_2 and thus it is considered a sustainable and environmentally friendly material due to no direct CO_2 release during manufacturing (Badogiannis et al., 2015; Baki et al., 2022). However, calcination of kaolin to produce reactive metakaolin has always been limited to temperatures below 900 °C due to the structural collapse of metakaolin and the abrasive nature of mullite crystals forming at around 1000 °C (Percival et al., 1974; Jämsä-Jounela et al., 2018). Impurities such as muscovite, a potassic mica mineral often found in kaolin, play a fluxing role in phase transformation dynamics, accelerating or decelerating the process (Lecomte et al., 2007; Zhou et al., 2013). On the other hand, the approximate temperature range at which muscovite begins to influence the structural reorganization of metakaolin remains uncertain. The

* Corresponding author. Micro and Nanotechnology Programme, Middle East Technical University, 06800, Ankara, Turkey.
E-mail address: paltay@metu.edu.tr (P. Pasabeyoglu).

https://doi.org/10.1016/j.jclepro.2023.137611
Received 27 March 2023; Received in revised form 12 May 2023; Accepted 28 May 2023
Available online 29 May 2023

delicate range between 900 and 1100 °C is of particular interest for determining the extent of metakaolin reactivity with newly crystalline phases formed like spinel and mullite (Lecomte and Blanchart, 2006).

$$Al_2O_3 \cdot 2SiO_2 \cdot 2H_2O \rightarrow Al_2O_3 \cdot 2SiO_2(\text{metakaolinite}) + 2H_2O \quad (1)$$

Metakaolin has emerged as a promising natural alternative to traditional high-purity chemicals for the green synthesis of zeolites in a sustainable and environmentally friendly manner (Hartati, 2020; He et al., 2021). Zeolites are microporous, crystalline, hydrous aluminosilicates of alkali and alkaline earth metals with a unique 3D structural framework composed of $[SiO_4]^{4-}$ and $[AlO_4]^{5-}$ tetrahedral units interconnected by shared oxygen (Indira and Abhitha, 2022). Among more than 230 zeolites, zeolite 4 A (LTA) and zeolite 13X (FAU) are the most commonly used types (Borai et al., 2009; Moshoeshoe et al., 2017; Martínez and L, 2019). Metakaolin has been proven to be a satisfactory precursor for zeolite 4 A synthesis since kaolin's chemical composition is well-suited for the process (Kirdeciler and Akata, 2020; Akinruli et al., 2021; Schwanke et al., 2022). However, zeolite 13X synthesis requires either an additional silica source or post-treatment of the clay. (Novembre et al., 2011; Garshasbi et al., 2017). Calcination conditions carried out to convert kaolin into metakaolin are known to affect the outcome directly. An example can be given as the formation of sodalite and zeolite A, zeolite A, and zeolite P at calcination temperatures of 500, 750, and 950 °C respectively, while calcination at 1050 °C did not retrieve any zeolite A (Imbert et al., 1994; Basaldella et al., 1998; Mohammadi and Pak, 2002). There had been other attempts at making zeolites using metakaolin calcined above 900 °C; however, desired forms of zeolites could not be obtained in most cases (Chandrasekhar, 1996). Some of the successful attempts resulted in the formation of zeolite 13X with low quality and yield (Flank, 1970; Basaldella et al., 1998). These results have demonstrated that the type of zeolite formed is highly dependent on metakaolin reactivity and thus the calcination temperature.

The calcination of kaolin in industry is commonly carried out using rotary kilns and multiple hearth furnaces (MHF) (Jämsä-Jounela et al., 2018). While this process does not produce harmful gases that pollute the environment, it requires a significant amount of energy, often derived from the combustion of fossil fuels such as oil or coal (Tasiopoulou et al., 2023). The high-temperature calcination is particularly energy-extensive, leading to industrial drawbacks. Furthermore, the high cost of production of metakaolin, which ranges from $600-$700 per ton, remains a challenge due to the limited number of production plants, lack of attention on the significance of sustainable practices, and risk of poorly implemented kaolin mining (Lehne and Preston, 2018; Bakera and Alexander, 2019). To address these challenges, researchers have explored alternative methods such as mechanochemical activation to reduce fossil fuel dependencies (Mitrović and Zdujić, 2013).

The use of concentrated solar thermal energy (CSTE) was proposed as another alternative process for calcination to provide the necessary thermal energy (Hanein et al., 2022). The impact of using concentrated solar thermal energy on the fuel and total emissions of metakaolin can be estimated based on literature values. Tasiopoulou et al. compared the calcination of metakaolin at various parameters such as temperature, moisture, fuel type, and process type (Tasiopoulou et al., 2023). Based on their findings and extrapolated to calcination at 950 °C, the fuel-related emissions are 301 kg CO_2/tonne metakaolin for operation with coal (lignite), whereas natural gas results in 191 kg CO_2/tonne metakaolin. By using CSTE, these emissions drop significantly to just 6 kg CO_2/tonne metakaolin, since CSTE provides a heat footprint of 6 kg/MWh and the process requires 1 MWh/tonne metakaolin at 950 °C (Renewable Energy Sources and Climate Change Mitigation: Special Report of the Intergovernmental Panel on Climate Change, 2011). Thus, fuel emissions could be reduced by over 97%. If the impact on the complete process and lifecycle of the production is assessed, again a drastic reduction can be found. Fig. 1 shows that the total lifecycle emissions with the coal process are 716 kg CO_2/tonne metakaolin. This number decreases to 541 CO_2/tonne metakaolin for natural gas and further to 289 CO_2/tonne metakaolin for CSTE. This represents a 60% reduction compared to coal and a 47% reduction compared to natural gas.

Solar reactors were already employed in lab-scale for different applications such as calcination of limestone, reduction of ZnO, steam gasification of petcoke, and thermal splitting of methane, reaching temperatures well above 1000 °C (Alonso and Romero, 2015). Likewise, solar rotary kilns were used for the treatment of powders, granules, and even scraps (Alonso et al., 2017). At the DLR, extensive expertise exists where solar rotary kilns and such reactors have already been tested for melting aluminum, reduction of cobalt oxide for thermochemical storage, and the calcination of cement raw meal (Neises et al., 2012; Alexopoulos et al., 2015; Moumin et al., 2019). Combining these aspects makes the technology highly attractive for the calcination of kaolin, as the process is industrially performed in rotary kilns or multiple hearth furnaces with temperatures in the range of 900–1000 °C. Accordingly, solarization of zeolite production with special emphasis on high-temperature calcination could further clarify this structural transformation of metakaolin, while providing a cleaner production route for zeolites.

This work aims to perform a proof-of-concept study of the calcination of kaolin in a solar rotary kiln at high temperatures and use the obtained metakaolin for zeolite production. Accordingly, the goal is to obtain one

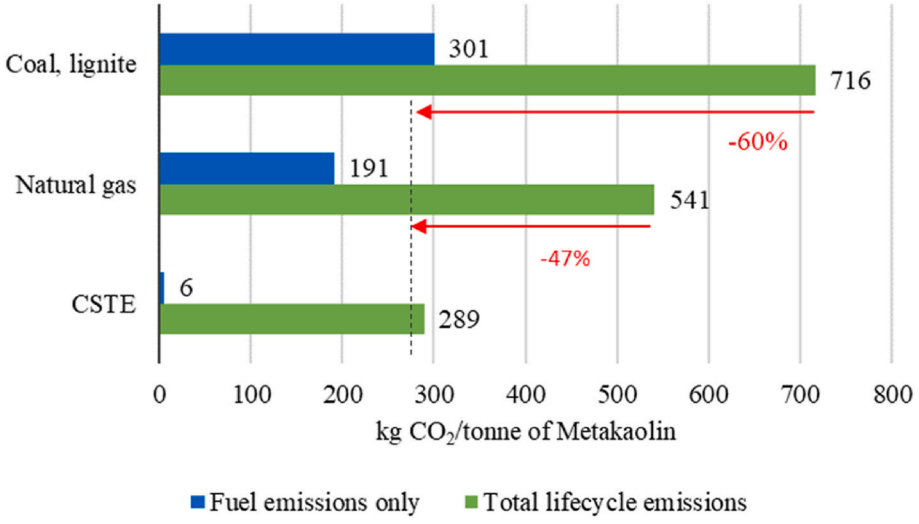

Fig. 1. Comparison of metakaolin production at 950 °C with coal (lignite), natural gas, and concentrated solar thermal energy (CSTE) based on data (Renewable Energy Sources and Climate Change Mitigation: Special Report of the Intergovernmental Panel on Climate Change, 2011; Tasiopoulou et al., 2023). Fuel emissions are shown in blue and total lifecycle emissions in green. (For interpretation of the references to colour in this figure legend, the reader is referred to the Web version of this article.)

of the most widely used metakaolin materials avoiding the need for burning fossil fuels. Meanwhile, metakaolin obtained from solar simulator-calcined kaolin at different calcination temperatures was investigated to synthesize zeolites. This paper presents an innovative method for obtaining the most essential commercial zeolite types, which are zeolite 4 A and zeolite 13X, without any pre- or post-treatment applied to the mother clay or the need for additional silica sources for zeolite 13X.

2. Materials and methods

2.1. Materials

The kaolin was obtained from Eczacıbaşı Esan Co Ltd., Turkey. The chemical composition of kaolin (K) measured and expressed in the form of oxides by XRF is given in Table 1. Kaolin is mainly constituted of silicon dioxide (46.1 wt%) and alumina (38.3 wt%). LOI (loss on ignition) was determined to be 12.5 wt% by TGA and Si/Al mol ratio was calculated to be 1.02.

Sodium hydroxide (NaOH) pellets were obtained from Sigma Aldrich Chemicals. Deionized water is distilled from running tap water with a water purification system (Milli-Q system, $\leq$18 Ω).

2.2. Solar simulator calcinations

The experiments were performed at the high flux solar simulator (HFSS) of the DLR, Cologne. The facility can provide up to 20 kW of thermal power at the focal plane and consists of 10 xenon short-arc lamps (Dibowski et al., 2007). The utilized reactor was previously tested successfully for sustainable nitrogen-based fertilizer production (Gaustad et al., 2019). A view of the simulator is shown in Fig. 2. The lamps are located on the right and two are operating in this case. The light is focused into the reactor on the left. Since the reactor is a cavity, most of the radiation is absorbed inside and heats up the reactor to temperatures up to 1000 °C. The simulator acts as a replacement for on-sun operations, where the sunlight is focused into the reactor with mirrors. This allows operations independent of the weather conditions and due to the light spectrum of the lamps being similar to the sunlight, a transfer of these results to on-sun operations is still possible.

The reactor was a rotary kiln, which was operated in batch mode. A CAD-drawing of the setup and a cut-view of the reactor is shown in Fig. 3. The reactor has an aperture opening of 80 mm in diameter. The inner crucible is made of high temperature steel 1.4828, having a diameter of 209 mm and a total length of 650 mm. High temperature blankets were used as insulation between the crucible and shell. The crucible volume is about 17 L while for the tests about 1.25 L of material were used, corresponding to 1 kg of kaolin.

A total of 9 type-K thermocouples were used to measure the temperatures inside and outside of the reactor (Fig. 3b). The positions of TC1–5 are at 28, 60, 230, 420, and 470 mm from the inlet while TC6 is fixed at the aperture and TC7 is fixed at the housing. TC8 and 9 are also located at about 60 mm from the inlet, as shown in Fig. 3b, to measure respectively the particle bed and gas temperature.

For the operation, the following procedure was employed: first, the kiln was filled with 1 kg of kaolin particles. The rotation was started at 3 rpm and the reactor was heated up step-wise with up to 7 lamps, corresponding to a maximum thermal power input of 5.6 kW. Once the desired temperature was reached, for which TC3 was taken as the reference, the power was either reduced or maintained to stay at this temperature for 2 h. Afterward, the lamps were shut off and the material was taken out of the kiln once it cooled down. In total, 10 tests were performed. Out of 10 tests, 6 are presented in this paper. Since TC8 was in contact with calcined kaolin, average temperatures of TC8 were selected to be given here. Samples calcined with solar simulators were named KSC-TC8avg (Table 2).

2.3. Zeolite synthesis

A typical hydrothermal synthesis protocol was applied based on a previous study (Kirdeciler and Akata, 2020). Calcined kaolin (metakaolin) was used as a source of both SiO_2 and Al_2O_3, with a zeolite gel formula of $2.04SiO_2$:$1Al_2O_3$:$3.14Na_2O$:$110H_2O$. The calculated amounts of NaOH and DDW were added to the metakolin to form the gel in a HDPE bottle. The resulting mixture was aged for 4 h at 60 °C in a water bath with continuous agitation at 400 rpm. Subsequently, the mixture was allowed to react for 4 h in a 100 °C preheated oven without agitation. The resulting solid particles were centrifuged at 5000 rpm for 5 min, washed 3 times with deionized water, and dried at 60 °C overnight. The samples were denoted as Z-KSC-X, where X represents the temperature of solar calcination.

2.4. Characterization

The chemical composition of kaolin was characterized by a Rigaku ZSX Primus II X-ray fluorescence spectrometer (XRF). The crystal structure transformation and the phase compositions of the kaolin, metakaolins and zeolite products were analyzed by X-ray diffraction (XRD) using a Rigaku Miniflex operating at 40 kV and 15 mA with Bragg-Brentano geometry, Ni filter and CuKα radiation. Qualitative and quantitative (WPPF) analyses of the samples were done by using SmartLab Studio II software equipped with PDF 4+ database. The percent crystallinity calculations of the synthesized zeolites were calculated from the XRD results using the software. Card # 04-009-4857 and card # 00-038-0240 were used as 100% crystallinity for Zeolite 4 A and Zeolite 13X, respectively. Crystallite sizes were calculated with Halder-Wagner method. The morphology of the kaolin, metakaolins, and zeolites was characterized by Field Emission Scanning Electron Microscope (FE-SEM) using an FEI Quanta 400 instrument. FTIR spectra were recorded at room temperature in the mid-IR spectral range 400–4000 cm^{-1} region at 4 cm^{-1} resolution accumulating 16 scans using a PerkinElmer 400 spectrometer equipped with diamond ATR (attenuated total reflectance). All the raw material and final product characterizations were performed in the Middle East Technical University (METU) Central Laboratory, Turkey.

3. Results and discussions

3.1. Solar experiments

Fig. 4 shows the temperature profile of the test named KSC-960 with the rotary kiln, where the envisioned temperature was 850 °C maintained for 2 h at TC3. The reactor was heated up step-wise, starting with 1 lamp and adding another lamp every 10 min. It can be seen that the initial temperatures inside the reactor were about 50 °C, being a result of heat stored from the experiment on the previous day. Once the lamps were turned on, the temperatures at the aperture (TC6) and the gas (TC9) increased the fastest, followed by the bed temperature (TC8). All other thermocouple measurements were lower than these values. Once 6 lamps were operating, the power was maintained to achieve the desired 850 °C at TC3. Afterward, one lamp was shut down to stay as close as

Table 1
Chemical composition of kaolin sample measured by XRF.

Oxides	SiO_2	Al_2O_3	K_2O	TiO_2	Fe_2O_3	CaO	MgO	LOI
Content (%)	46.1	38.3	0.885	0.814	0.590	0.373	0.142	12.5

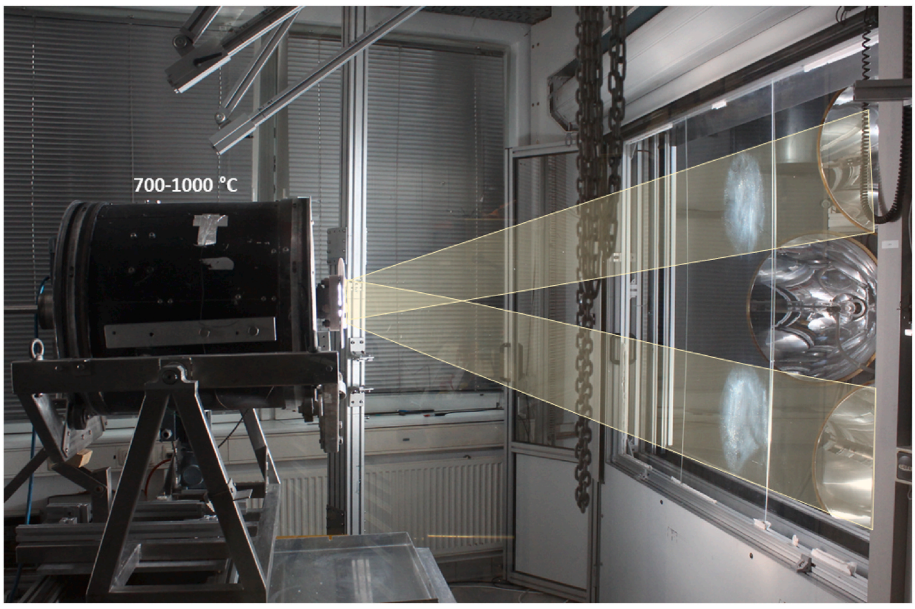

Fig. 2. Experimental setup of the solar reactor and solar simulator.

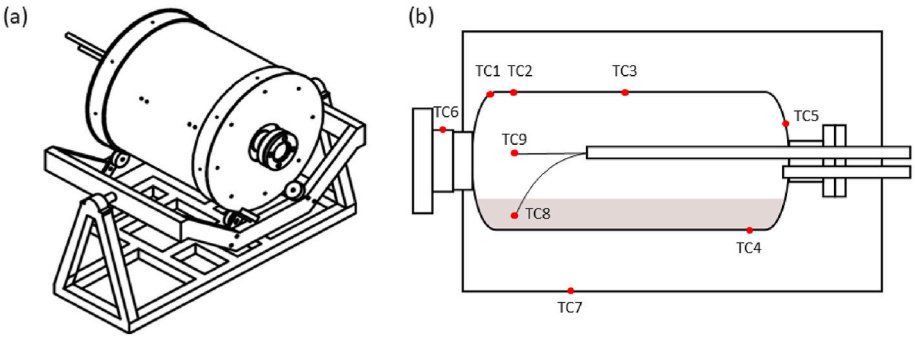

Fig. 3. Schematic diagram of the solar reactor (a) and construction of the tubular reactor with thermocouples (TC) (b).

Table 2
Sample names and thermocouple (TC) measurements during calcination.

Sample Name	TC8start	TC8max	TC8avg	TC3start	TC3max	TC3avg
KSC-740	600	760	740	550	650	640
KSC-800	780	805	800	650	750	700
KSC-860	860	910	860	750	800	760
KSC-940			940[a]	850	850	850
KSC-960	980	1000	960	850	890	870
KSC-980	1000	1000	980	900	980	950

[a] An estimate of TC8 measurement data was reported based on furnace tests.

possible to this temperature. During calcination, TC3 temperature slightly deviated from 850 °C to a maximum of 890 °C, giving an average TC3 temperature of 870 °C. After 2 h at the required temperature level, all lamps were shut down and the experiment was completed. A rapid decrease was seen for all temperatures after the shutdown. During the whole experiment, the outer shell temperature (TC7) reached a maximum value of 76 °C.

Since the bed temperature (TC8) was critical for determining the reactivity of metakaolin for zeolite synthesis, its correct prediction and thus the power needed to reach that temperature was of key importance. In general, TC8 was about 100 °C higher than the outer surface of the crucible (TC3), which was used as the reference for the tests. Furthermore, a temperature drop was seen in the range of 550–600 °C, which was in line with the endothermic dehydroxylation reaction temperature of kaolin occurring in the range of 450–700 °C (Teklay et al., 2014):

The unique behavior of TC8 showing the dehydroxylation in operando was the reason for samples to be named after accurate TC8 temperature measurements. After about 2 h, the bed reached a constant temperature as mentioned by the values reported as TC8avg for each experiment performed at 6 different temperatures (Table 2). These temperatures were taken as reference values during the performance of conventional experiments.

3.2. Characterization of the kaolin and metakaolins

The XRD pattern of kaolin that was used in this study was illustrated in Fig. 5a. Kaolinite was characterized by major peaks appearing at 12.34° (2θ) and 24.88° (2θ) with d-spacings of 7.16 and 3.58 Å, corresponding to the (001) and (002) reflection planes, respectively (Card # 01-080-0885). In addition to kaolinite, the XRD pattern of kaolin also showed the reflection peaks of quartz (Card # 01-089-8937) and muscovite (Card # 07–0042) as impurities. The presence of muscovite in the XRD pattern of the kaolin is consistent with the K_2O content obtained from the chemical analysis of the mineral (Table 1). Whole-powder-pattern fitting (WPPF) analysis on kaolin revealed that the kaolin sample contained over 96 wt% kaolinite, indicating high-purity kaolin. The Hinckley index (HI), which is used to differentiate between low and high-defect kaolinites based on their crystallinity was calculated from the XRD pattern (Hinckley, 1962). The HI value

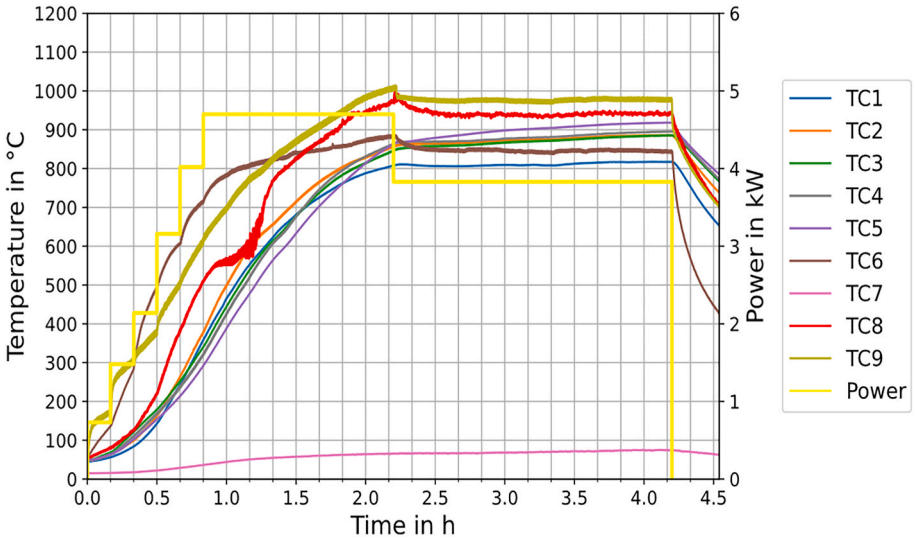

Fig. 4. Solar calcination temperature profile of KSC-960. The envisioned temperature was 850 °C at TC3. The thermal power belongs to the secondary axis.

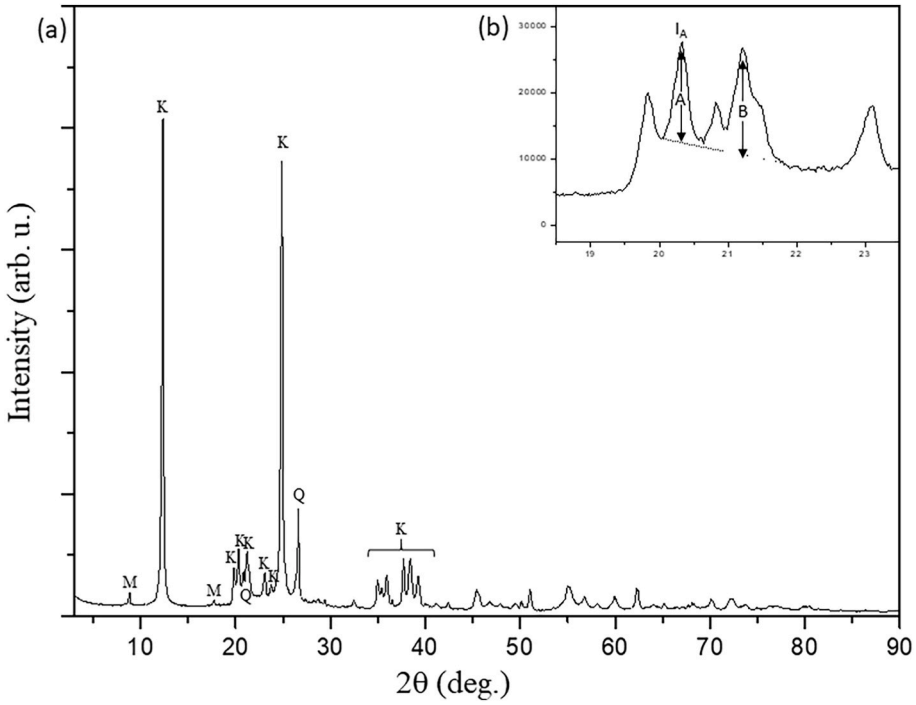

Fig. 5. XRD pattern of kaolin (a) and Hinckley index region for the determination of values for the calculation of HI (M: Muscovite, K: Kaolinite, Q: Quartz) (b).

obtained for the kaolin sample was 1.37 (Fig. 5b), indicating a low defect and high structural order of kaolinite.

Fig. 6 shows the scanning electron micrographs of the kaolin and metakaolins. The stacked layered and booklet morphology of kaolinite aggregates in kaolin was observed in Fig. 6a. As calcination progressed, the lamellar structure of kaolinite turned into highly disordered metakaolin with a sheet-like morphology (Fig. 6b–f). The micrographs show the randomly oriented amorphous plates of metakaolin with particle size fractions between 2 and 5 μm. SEM images were consistent and comparable with the literature (Salih et al., 2020; Sazali and Harun, 2022). Mullite, which is generally identified by its very characteristic needle-like microstructure, was not observed even at the highest calcination temperature of 980 °C (SI-1) (Soares et al., 2007). These results are in agreement with the reported data indicating that although there is no general agreement on the phase transformation route of kaolinite to mullite, crystalline mullite forms at temperatures higher than 1000 °C, which was not exceeded in the current study (Zhou et al., 2013).

The XRD patterns of the metakaolins (Fig. 7a) showed the diffuse halo structure between 15 and 36° (2θ) corresponding to the formation of amorphous metakaolin, which was suggested to be composed of free silica containing alumina or silica-rich alumina phases (Chakraborty et al., 2003). The absence of kaolinite peaks indicated that the kaolin was fully transformed into metakaolin. The intensity of the muscovite peak did not change significantly up to 860 °C but started to diminish as the temperature increased to 940 and 960 °C. At 980 °C, the muscovite peak completely disappeared (Fig. 7c). The quartz peaks did not show any changes in intensity with increasing calcination temperature (Fig. 7d). These results suggest that muscovite decomposed at high temperatures without any decomposition of quartz as impurities. Furthermore, as the calcination temperature increased to 940 °C,

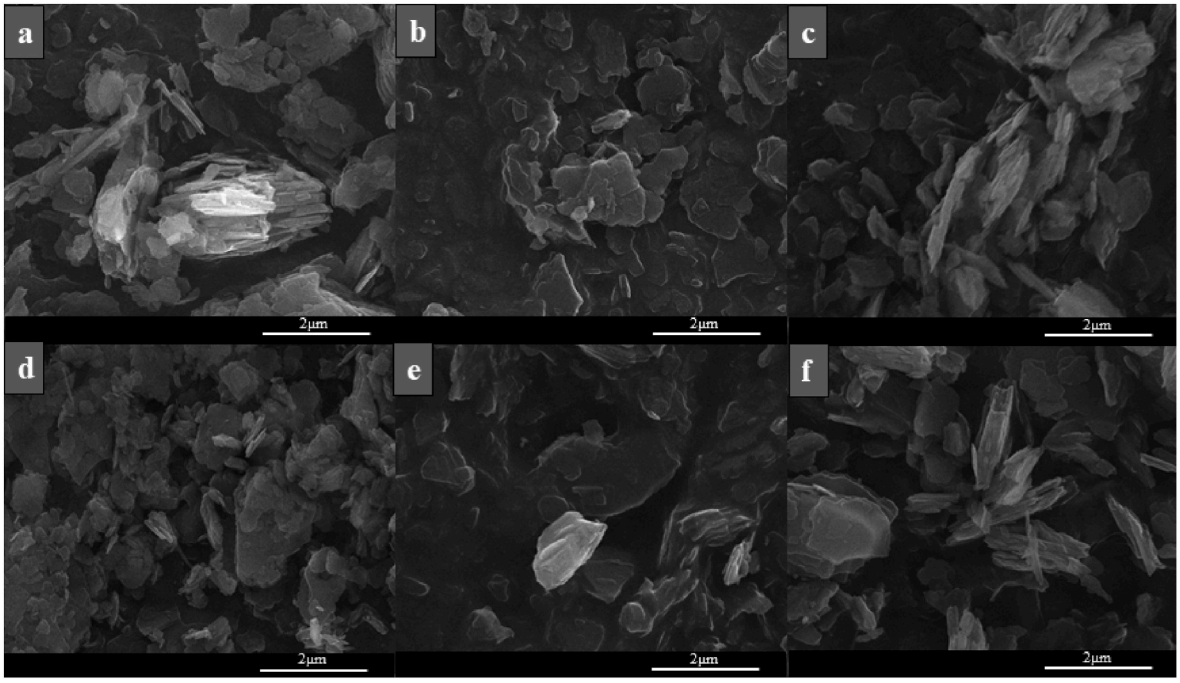

Fig. 6. SEM images of kaolin (a), KSC-740 (b), KSC-800 (c), KSC-860 (d), KSC-940 (e), and KSC-960 (f).

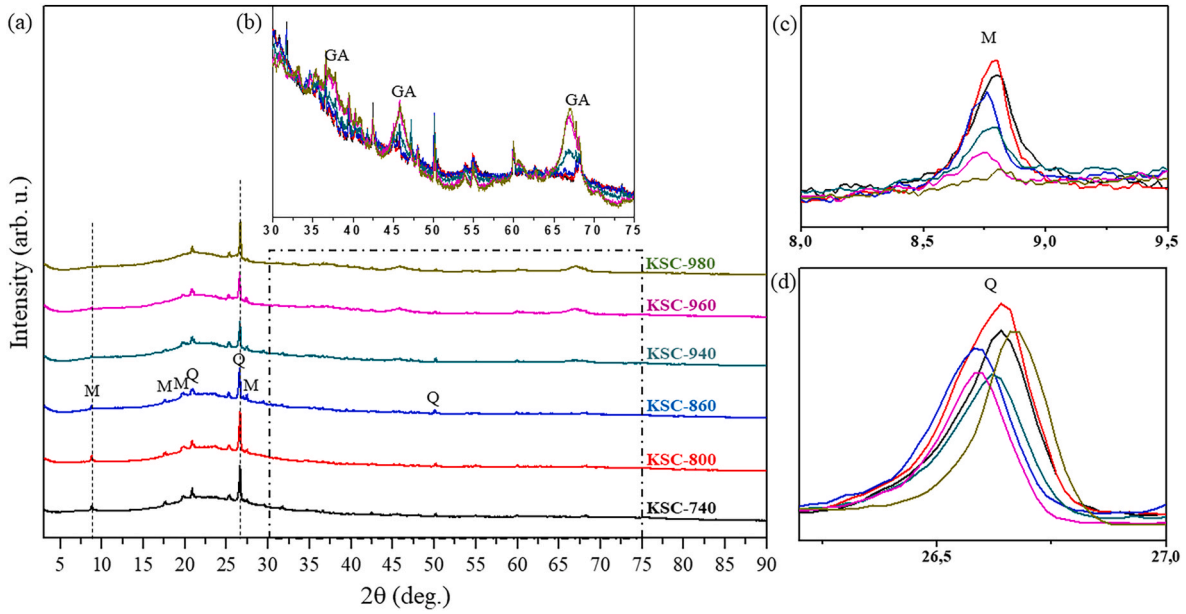

Fig. 7. XRD patterns of metakaolins (a) and zoomed-in regions to show Al–Si spinel (GA: gamma alumina) formation (b), muscovite major peak (c) and quartz major peak (d) (M: Muscovite, Q: Quartz).

nanocrystallites (Halder-Wagner crystallite size of 4.04 nm) of Al–Si spinel (gamma-alumina type) started to form (marked as GA in Fig. 6b), appearing at 37.4°, 45.90°, and 66.94°, that matches with (311), (400) and (440) planes of gamma alumina with a cubic structure (Card # 04-016-1445), respectively (Urbonavicius et al., 2020). These results indicate that there is an influence of muscovite on the structural reorganization of metakaolin above 900 °C, leading to the formation of Al–Si spinel (Fig. 6b) and amorphous silica, without the formation of mullite. This transition was not as significant until 940 °C, suggesting the final reactivity of metakaolin would be different for metakaolin samples calcined above this temperature. These results are consistent with literature stating that muscovite in kaolin can modify the decomposition of kaolinite and delay the formation of mullite (Zhou et al., 2013).

The FTIR spectrum of the kaolin is shown in Fig. 8a. The characteristic absorption bands of kaolinite were located between 3500 and 3750 cm^{-1}, which correspond to the stretching frequencies of OH groups (Madejová, 2003). Four distinct bands were observed at 3687, 3670, 3650, and 3620 cm^{-1} indicating an ordered structure of kaolinite (Bich, 2005). This result supports the high Hinckley index value calculated from the XRD pattern in Fig. 5b. The OH deformation bands of kaolinite were detected at 938 and 913 cm^{-1} as well as minor bands for Si–O at 1115, 794, and 684 cm^{-1} (Feriancová et al., 2021). The peaks at 1025 and 1000 cm^{-1} were assigned to the stretching vibration of the external and in-plane Si–O groups, while the signals at 793 and 752

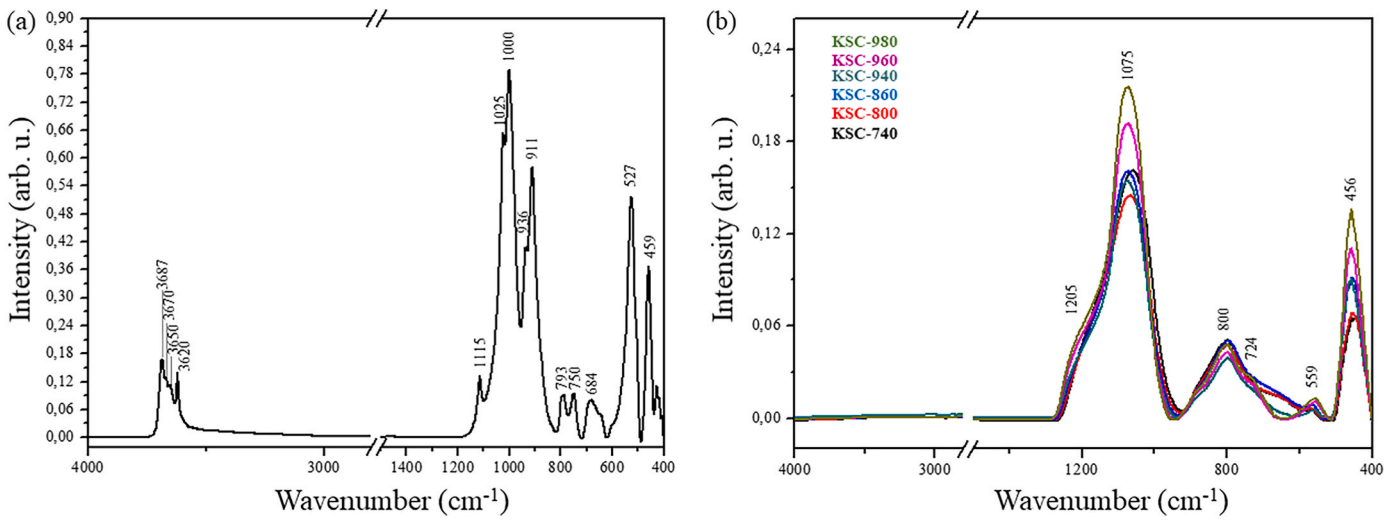

Fig. 8. FT-IR spectra of kaolin (a) and solar calcined kaolins (b).

cm^{-1} were assigned as symmetric vibrations of Si–O–Si bonds (Saikia et al., 2003).

In the FT-IR spectra of the solar calcined kaolin samples presented in Fig. 8b, the absence of OH groups between 3500 and 3750 cm^{-1} confirmed the dehydroxylation of kaolinite into a reactive amorphous phase through calcination. The major peak around 1075 cm^{-1} was assigned to the antisymmetric stretching mode of Si–O–Al, and its absorption intensity increased with increasing calcination temperature. This suggests the formation of amorphous silica, and the bandwidth expansion is attributed to the higher variation of energy in the Si–O–Si bonds. The shoulder of the band around 1205 cm^{-1} was assigned to the antisymmetric stretching mode of Si–O–Si of (SiO_4) tetrahedra. As the calcination temperature increased and Al–Si spinel formation occurred, this shoulder became more prominent. The peak around 800 cm^{-1} was assigned to Al–O bond stretching of (AlO_4) tetrahedra and it had two features located at 882 and 724 cm^{-1}. The peak around 559 cm^{-1} was assigned to Al–O bond stretching of (AlO_6) octahedra and the bending mode of (SiO_4) tetrahedra can be observed at 456 cm^{-1}, with the intensities of both increasing as the calcination temperature increased. The presence of Al atoms occupying both the tetrahedral and octahedral sites as the calcination temperature increases, as shown by Ptáček et al. is another indication of the formation of the Al–Si spinel phase (Ptáček et al., 2011).

3.3. Characterization of the zeolites

The morphology of the zeolite products synthesized from solar-calcined kaolin at different temperatures was shown in Fig. 9. The SEM micrographs of the zeolites synthesized from kaolin calcined at 740, 800, and 860 °C (Fig. 9a, b, c) showed the formation of cubic crystals with smooth surfaces, with an approximate size of 2 μm, and characteristics of the LTA structure (Sharma et al., 2012). However, as the solar calcination temperature increased to 940 °C, a mixture of zeolite 4 A and 13X was formed with smaller particle size (Fig. 9d). For

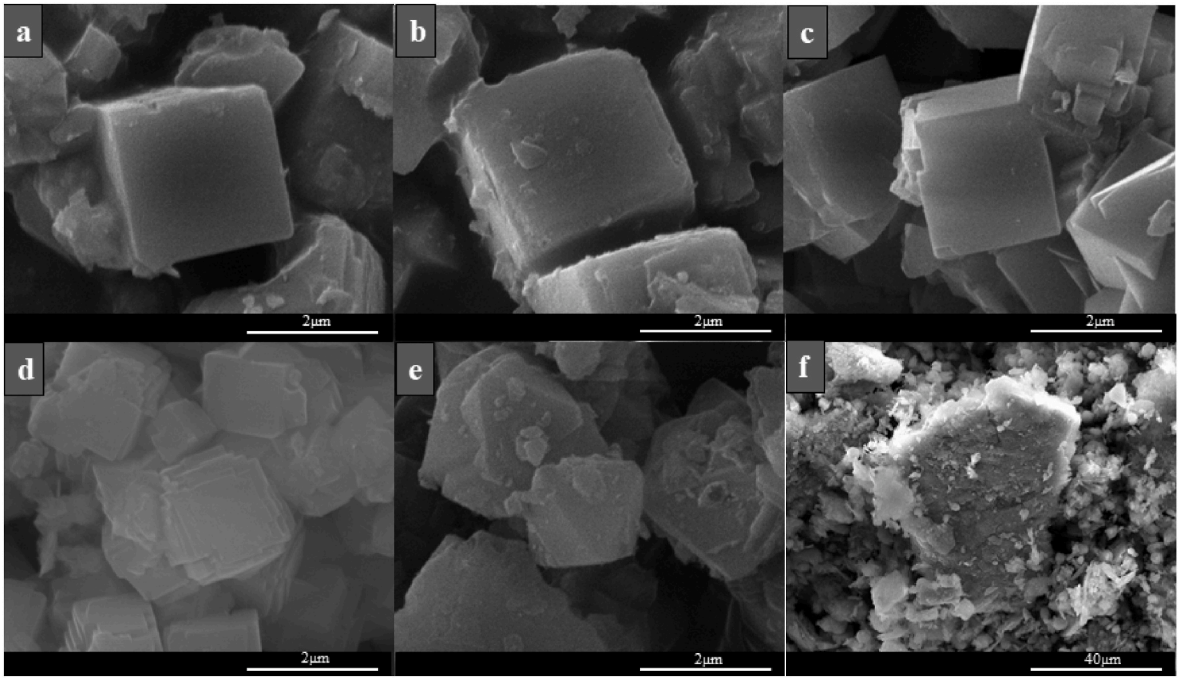

Fig. 9. SEM images of Z-KSC-740 (a), Z-KSC-800 (b), Z-KSC-860 (c), Z-KSC-940 (d), Z-KSC-960 (e), and Z-KSC-980 (f).

the Z-KSC-940 sample, cubic crystals of zeolite 4 A in Fig. 9d were observed to be deformed with deteriorated sharp cubic edges. At a solar calcination temperature of 960 °C, octahedral crystalline form of zeolite 13X was observed in the SEM image for Z-KSC-960 indicating a complete transformation of 4 A to 13X (Fig. 9e) (Zhou et al., 2013). The particle size of the Z-KSC-960 was estimated to be around 1–3 μm, which was in good agreement with the literature (Ma et al., 2014). Finally, at a solar calcination temperature of 980 °C (Fig. 9f), no zeolitic structures were observed, and large chunks of unreacted debris were visible in the SEM image indicating synthesis failure.

The XRD patterns of the zeolite products synthesized from solar-calcined kaolin are shown in Fig. 10. The products synthesized from kaolin calcined at 740, 800, and 860 °C resulted in high-quality zeolite 4 A products, with over 94% crystallinity and quartz as the only impurity, present at a level below 5 wt%. Interestingly, the quality of the zeolites synthesized from fully metakaolin samples obtained at these temperatures was found to be almost identical. These findings suggest that good-quality zeolite 4 A can be synthesized from metakaolins obtained from a wide range of calcination temperatures using solar reactors.

As the solar calcination temperature increased to 940 °C, a mixture of zeolite 4 A and zeolite 13X was obtained for Z-KSC-940 (Fig. 10), which correlated well with SEM results (Fig. 9d). The quantitative phase analysis (QPA) conducted by WPPF method is shown in Fig. 11a. Accordingly, the mixture consisted of 59 wt% zeolite 13X and 41 wt% zeolite 4 A using KSC-940 as a precursor material for the synthesis. Interestingly, a further increase in calcination temperature to 960 °C resulted in zeolite 13X with no zeolite 4 A formation. The QPA analysis also showed that an additional increase in calcination temperature led to a complete transformation of 4 A to 13X phase (Fig. 11a). The evolution of percent crystallinity values showed a similar trend with QPA analysis results, indicating well-crystallized zeolite 4 A products (~94%) for Z-KSC-740, 800 and 860 samples, and pure zeolite 13X (Z-KSC-960) transformed from zeolite 4 A with ~91.4% crystallinity (Fig. 11b). For the Z-KSC-940 sample, obtained percent crystallinity values were 62.4% for zeolite 13X and 56.6% for zeolite 4 A, which were very low compared to the other synthesized samples.

Crystallite sizes calculated using Halder-Wagner method for the blend sample of Z-KSC-940 were 41.3 nm for zeolite 4 A and 44.1 nm for zeolite 13X (SI-5). These values were lower than those observed in pure zeolite samples, such as zeolite 4 A (Z-KSC-740/800/860) and zeolite 13X samples (Z-KSC-960), which had average crystallite sizes of 49.1 and 46.4 nm respectively (SI-2-3-4 and SI-6). The coexistence of zeolites 13X and 4 A in the product obtained at 940 °C can be attributed to different nucleation and crystal growth mechanisms. In such cases, nucleation takes place inside the gel followed by crystal growth for LTA, while nucleation begins on the exterior surface and crystals grow by consuming the amorphous material for FAU at increased calcination temperatures (Oleksiak et al., 2016). The calculated decrease in crystallite size for the blend sample obtained at 940 °C may also be indicative of competition between nucleation and crystal growth during a transformation from zeolite 4 A to 13X. These results suggest an inter-crystalline transformation of LTA (4 A) to FAU (13X) at elevated calcination temperature of kaolin for the first time.

Murat et al. investigated zeolite synthesis from two kaolinite samples calcined at a temperature range of 600–1100 °C differing in their structural iron content and crystallinity with some muscovite content (Murat et al., 1992). The study found that the transformation of zeolite A to zeolite P, which is a thermodynamically more stable version of zeolite 13X, occurred only for kaolin samples calcined above 900 °C. However, a mixture of Zeolite A and zeolite P was not obtained in the same study. In addition to the muscovite presence promoting the formation of zeolite P, free amorphous silica formation with Al–Si spinel formation happening at 925–1050 °C was also suggested to be the main reason for the zeolite P formation at higher temperatures. In the current study, the transformation from zeolite 4 A to zeolite 13X in high purity was obtained for the first time with the clear formation of the intermediate mixture sample of zeolite 4 A and 13X. Furthermore, the transformation from 4 A to 13X was found to be in agreement with the formation of Al–Si spinel (GA) as shown in Fig. 7b.

The formation of Al–Si spinel during calcination of metakaolin can have a profound effect on zeolite synthesis due to the loss of readily available alumina and the release of amorphous silica. Since its discovery in 1959 by Brindley and Nakahira (Brindley and Nakahira, 1959), silicon amount in Al–Si spinel is still much debated. While many researchers propose a pure gamma alumina model for the aforementioned spinel (Percival et al., 1974; Leonard, 1977; MacKenzie et al., 1985), others have calculated varying amounts of silicon, ranging between 3.9 and 11.5 wt% using different techniques (Okada, 1986; Okada and Otsuka, 1986; Sonuparlak et al., 1987; MacKenzie et al., 1996). A recent study by Wallez et al. suggested that Al–Si spinel has all the

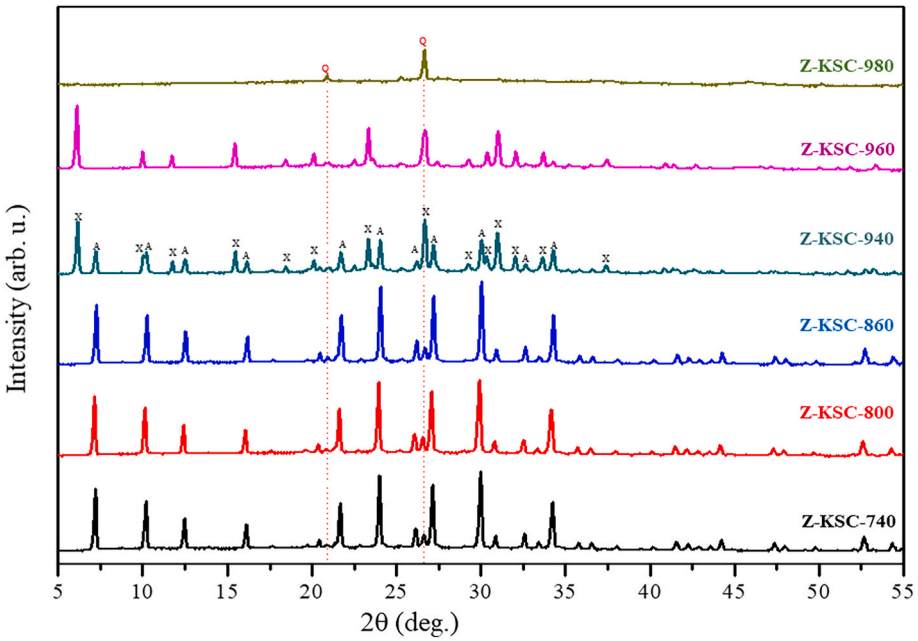

Fig. 10. XRD patterns of the synthesized zeolites Z-KSC-740/800/860/940/960/980 (X: Zeolite 13X, A: Zeolite 4 A, Q: Quartz).

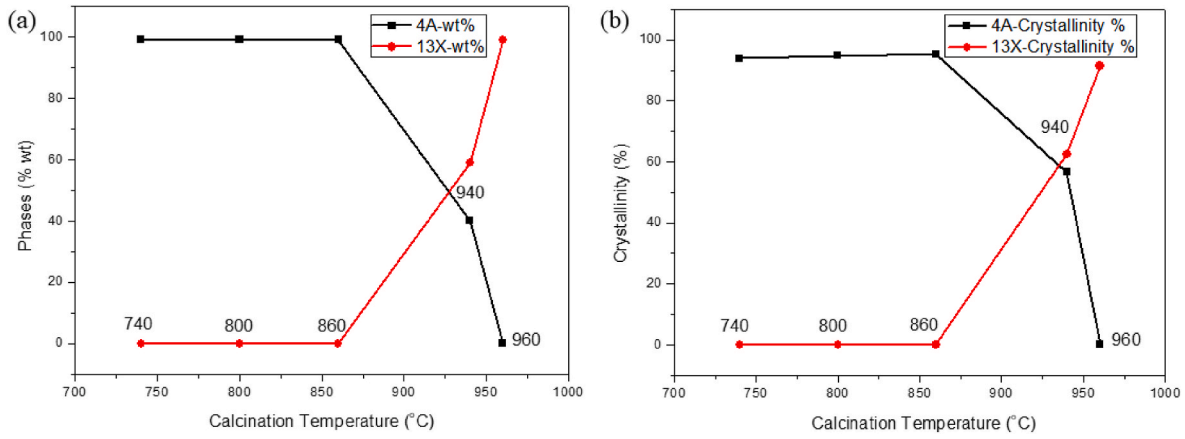

Fig. 11. Weight fractional (a) and percent crystallinity changes of zeolite phases as a function of calcination.

characteristics of a transition alumina form with uniform cell volume and a 5 nm crystallite size with a cubic structure (Chauffeton and Wallez, 2022). Additionally, the rate of Al–Si spinel formation has been shown to decrease with increasing heating rate (Ptáček et al., 2010). Although previous research has shed light on the formation of Al–Si spinel during calcination, this study emphasizes its crucial role in zeolite synthesis and highlights the need to carefully control its formation to achieve the desired product.

The current study demonstrated that solar calcination of kaolin can successfully produce zeolite 4 A upon up to ~940 °C without the need for precise control of reactor temperature, with the formation of zeolite 13X achieved above this temperature. The role of Al–Si spinel (gamma alumina) and muscovite decomposition, as well as the formation of reactive amorphous silica, played a significant role in the transformation to zeolite 13X. Accordingly, an alternative processing route using solar calcination of kaolin was shown to be successful for making zeolite 4 A and zeolite 13X using metakaolin formed at different calcination temperatures with less energy consumption and fewer CO_2 emission compared to traditional methods. In a future paper, we will discuss in more detail the practical applications of these solar-processed zeolites and their potential use as effective CO_2 adsorbents.

4. Conclusion

In this study, a new solar calcination route was introduced using solar-heated rotary kiln to produce metakaolin in a wide temperature range of 700–1000 °C. The metakaolin obtained using low and high solar calcination temperatures was then used as a precursor for the synthesis of zeolite 4 A and 13X respectively, without any additional silica source or post-treatment of the clay. The results demonstrate the potential of using natural low-cost clay compounds like kaolin to perform high-temperature solar calcination in an energy and cost-effective manner. Key findings from the study are as follows.

(1) Zeolite 4 A was achieved with above 90% crystallinity for all products irrespective of the metakaolinization temperature (740–860 °C).
(2) At a high temperature of ~940 °C, zeolite 13X was formed via a transition state and partial formation of Al–Si-spinel (gamma-alumina type), resulting in a product mixture of zeolite 4 A and zeolite 13X.
(3) Further increasing the calcination temperature to ~960 °C resulted in pure zeolite 13X with high crystallinity.
(4) No zeolite formation was observed at a calcination temperature of 980 °C, probably due to the total decomposition of metakaolin.

The findings of this study reveal that the disappearance of muscovite and the formation of Al–Si spinel align with the transformation from zeolite 4 A to 13X. This suggests that there is an influence of muscovite on the structural reorganization of metakaolin above 900 °C, above which the final reactivity of metakaolin can be affected for its potential use as a precursor during zeolite synthesis. The results underscore the importance of a delicate temperature range where Al–Si spinel phase and amorphous silica formation occur to obtain zeolite 13X with good crystallinity. While the results demonstrate the potential of solarization in zeolite production, particularly in the context of the growing demand for cleaner energy sources, there may be limitations to using industrialized CSTE to control the precision of the temperature range where the metakaolin transformations might occur. Furthermore, the possible challenges associated with the construction of solar facilities and optimization of heliostats, as well as the limited availability of land area with sufficient solar radiation in regions with kaolin, need to be addressed to ensure the widespread adoption of this technology.

CRediT authorship contribution statement

Pelin Pasabeyoglu: Conceptualization, Methodology, Formal analysis, Investigation, Validation, Visualization, Writing – original draft, Writing – review & editing. **Gkiokchan Moumin:** Conceptualization. **Lamark de Oliveira:** Methodology, Formal analysis, Investigation, Validation. **Martin Roeb:** Conceptualization, Methodology, Resources, Supervision, Project administration, Funding acquisition. **Burcu Akata:** Conceptualization, Methodology, Resources, Writing – original draft, Writing – review & editing, Supervision, Project administration, Funding acquisition.

Declaration of competing interest

The authors declare that they have no known competing financial interests or personal relationships that could have appeared to influence the work reported in this paper.

Data availability

Data will be made available on request.

Acknowledgements

This project has received funding from the European Union's Horizon 2020 Research and Innovation programme under grant agreement n°823802. The support provided by METU-Central Laboratory is greatly acknowledged.

Appendix A. Supplementary data

Supplementary data to this article can be found online at https://doi.org/10.1016/j.jclepro.2023.137611.

References

Akinruli, I.J., et al., 2021. Synthesis and characterization of NaA zeolite using natural kaolinite clays from Nigeria by low temperature hydrothermal method. Int. J. Res. Eng. Sci. Manag. 4 (2), 40–47. https://doi.org/10.47607/ijresm.2021.498. Available at:

Alexopoulos, S.O., et al., 2015. Simulation model for the transient process behaviour of solar aluminium recycling in a rotary kiln. Appl. Therm. Eng. 78, 387–396. https://doi.org/10.1016/j.applthermaleng.2015.01.007. Available at:

Alonso, E., Romero, M., 2015. Review of experimental investigation on directly irradiated particles solar reactors. Renew. Sustain. Energy Rev. 41, 53–67. https://doi.org/10.1016/j.rser.2014.08.027. Available at:

Alonso, E., et al., 2017. Use of rotary kilns for solar thermal applications: review of developed studies and analysis of their potential. Sol. Energy 144, 90–104. https://doi.org/10.1016/j.solener.2017.01.004. Available at:

Badogiannis, E.G., et al., 2015. Durability of metakaolin self-compacting concrete. Construct. Build. Mater. 82, 133–141. https://doi.org/10.1016/j.conbuildmat.2015.02.023. Available at:

Bakera, A.T., Alexander, M.G., 2019. Use of metakaolin as a supplementary cementitious material in concrete, with a focus on durability properties. RILEM Techn. Lett. 4, 89–102. https://doi.org/10.21809/rilemtechlett.2019.94. Available at:

Baki, V.A., et al., 2022. The impact of mechanochemical activation on the physicochemical properties and pozzolanic reactivity of kaolinite, muscovite and montmorillonite. Cement Concr. Res. 162 (May), 106962 https://doi.org/10.1016/j.cemconres.2022.106962. Available at:

Basaldella, E.I., Sánchez, R.M.T., Tara, J.C., 1998. Iron influence in the aluminosilicate zeolites synthesis. Clay Clay Miner. 46 (5), 481–486. https://doi.org/10.1346/CCMN.1998.0460501. Available at:

Bergaya, F., Theng, B.K.G., Lagaly, G., 2006. Handbook of clay science. Available at: Dev. Clay Sci. https://doi.org/10.1016/S1572-4352(05)01039-1.

Bich, C., 2005. Contribution à l'étude de l'activation thermique du kaolin : évolution de la structure cristallographique et activité pouzzolanique. Institut National des Sciences Appliqués de Lyon, France.

Borai, E.H., et al., 2009. Efficient removal of cesium from low-level radioactive liquid waste using natural and impregnated zeolite minerals. J. Hazard Mater. 172 (1), 416–422. https://doi.org/10.1016/j.jhazmat.2009.07.033. Available at:

Brindley, G.W., Nakahira, M., 1959. The kaolinite-mullite reaction series: III, the high-temperature phases. J. Am. Ceram. Soc. 42 (7), 319–324.

Castelein, O., et al., 2001. The influence of heating rate on the thermal behaviour and mullite formation from a kaolin raw material. Ceram. Int. 27, 517–522. https://doi.org/10.1016/S0272-8842(00)00110-3. Available at:

Chakraborty, A., Das, S., Gupta, S., 2003. Evidence for two stage mullite formation during thermal decomposition of kaolinite. Br. Ceram. Trans. 102 (4), 153–157. https://doi.org/10.1179/096797803225004972. Available at:

Chandrasekhar, S., 1996. Influence of metakaolinization temperature on the formation of zeolite 4A from kaolin. Clay Miner. 31, 253–261.

Chauffeton, C., Wallez, G., 2022. Crystal-chemical investigation of the "cubic Al–Si spinel" issued from the thermal transformation of kaolinite and halloysite. J. Am. Ceram. Soc. 105 (7), 4986–4993. https://doi.org/10.1111/jace.18439. Available at:

Cheng, Y., et al., 2019. Dehydroxylation and structural distortion of kaolinite as a high-temperature sorbent in the furnace. Minerals 9 (10), 1–18. https://doi.org/10.3390/min9100587. Available at:

Dibowski, G., et al., 2007. Der neue Hochleistungsstrahler des DLR - Grundlagen. Anwendung', SonnenKolloquium Köln, Technik ([Preprint]).

Feriancová, A., et al., 2021. 'Preparation and application of modified organo-kaolinite by microwave-assisted irradiation'. Available at: Appl. Clay Sci. 213 https://doi.org/10.1016/j.clay.2021.106259.

Flank, W.H., 1970. 'Faujasite production', United States patent office. USA. https://patentimages.storage.googleapis.com/ff/ae/1c/564b0e85f929ea/US3515511.pdf.

Garshasbi, V., Jahangiri, M., Anbia, M., 2017. Equilibrium CO 2 adsorption on zeolite 13X prepared from natural clays. Appl. Surf. Sci. 393, 225–233. https://doi.org/10.1016/j.apsusc.2016.09.161. Available at:

Gaustad, G., et al., 2019. REWAS 2019: Manufacturing the Circular Materials Economy.

Hanein, T., et al., 2022. Clay calcination technology: state-of-the-art review by the RILEM TC 282-CCL. Mater. Struct. 55 (1) https://doi.org/10.1617/s11527-021-01807-6. Available at:

Hartati, et al., 2020. A review on synthesis of kaolin-based zeolite and the effect of impurities. J. Chin. Chem. Soc. 67 (6), 911–936. https://doi.org/10.1002/jccs.201900047. Available at:

He, Y., et al., 2021. Research progress on green synthesis of various high-purity zeolites from natural material-kaolin. J. Clean. Prod. 306, 127248 https://doi.org/10.1016/j.jclepro.2021.127248. Available at:

Hinckley, D.N., 1962. Variability in "crystallinity" values among the kaolin deposits of the coastal plain of Georgia and South Carolina. Clay Clay Miner. 11 (1), 229–235. https://doi.org/10.1346/CCMN.1962.0110122. Available at:

Imbert, F.E., et al., 1994. Venezuelan natural alumosilicates as a feedstock in the synthesis of zeolite A. Zeolites 14 (5), 374–378. https://doi.org/10.1016/0144-2449(94)90112-0. Available at:

Indira, V., Abhitha, K., 2022. A review on recent developments in Zeolite A synthesis for improved carbon dioxide capture: implications for the water-energy nexus. Energy Nexus 7 (June), 100095. https://doi.org/10.1016/j.nexus.2022.100095. Available at:

Irfan Khan, M., et al., 2017. The pyrolysis kinetics of the conversion of Malaysian kaolin to metakaolin. Appl. Clay Sci. 146 (May), 152–161. https://doi.org/10.1016/j.clay.2017.05.017. Available at:

Jämsä-Jounela, S.L., et al., 2018. Control strategy for a multiple hearth furnace in kaolin production. Control Eng. Pract. 81 (September), 18–27. https://doi.org/10.1016/j.conengprac.2018.08.020. Available at:

Khaled, Z., et al., 2023. Optimization of kaolin into Metakaolin: calcination Conditions, mix design and curing temperature to develop alkali activated binder. Ain Shams Eng. J. 14 (6), 102142 https://doi.org/10.1016/j.asej.2023.102142. Available at:

Kirdeciler, S.K., Akata, B., 2020. One pot fusion route for the synthesis of zeolite 4A using kaolin. Adv. Powder Technol. 31 (10), 4336–4343. https://doi.org/10.1016/j.apt.2020.09.012. Available at:

Lecomte, G., Blanchart, P., 2006. Textured mullite at muscovite-kaolinite interface. J. Mater. Sci. 41 (15), 4937–4943. https://doi.org/10.1007/s10853-006-0320-4. Available at:

Lecomte, G.L., Bonnet, J.P., Blanchart, P., 2007. A study of the influence of muscovite on the thermal transformations of kaolinite from room temperature up to 1,100 °c. J. Mater. Sci. 42 (20), 8745–8752. https://doi.org/10.1007/s10853-006-0192-7. Available at:

Lehne, J., Preston, F., 2018. Making Concrete Change Innovation in Low-Carbon Cement and Concrete. The Royal Institute of International Affairs, Chatham House Report Series.', p. 138. https://www.chathamhouse.org/2018/06/making-concrete-change-innovation-low-carbon-cement-and-concrete.

Leonard, A.J., 1977. Structural analysis of the transition phases in the kaolinite-mullite thermal sequence. J. Am. Ceram. Soc. 60 (1–2), 37–43. https://doi.org/10.1111/j.1151-2916.1977.tb16089.x. Available at:

Ma, Y., et al., 2014. Synthesis and characterization of 13X zeolite from low-grade natural kaolin. Adv. Powder Technol. 25 (2), 495–499. https://doi.org/10.1016/j.apt.2013.08.002. Available at:

MacKenzie, K.J.D., et al., 1985. Outstanding problems in the kaolinite-mullite reaction sequence investigated by 29Si and 27Al solid-state nuclear magnetic resonance: I, metakaolinite. J. Am. Ceram. Soc. 68 (6), 293–297. https://doi.org/10.1111/j.1151-2916.1985.tb15228.x. Available at:

MacKenzie, K.J.D., Hartman, J.S., Okada, K., 1996. MAS NMR evidence for the presence of silicon in the alumina spinel from thermally transformed kaolinite. J. Am. Ceram. Soc. 79 (11), 2980–2982. https://doi.org/10.1111/j.1151-2916.1996.tb08738.x. Available at:

Madejová, J., 2003. FTIR techniques in clay mineral studies. Vib. Spectrosc. 31 (1), 1–10. https://doi.org/10.1016/S0924-2031(02)00065-6. Available at:

Martínez, T., L, M., 2019. 'Synthesis and Identification Methods for Zeolites and MOFs', Zeolites and Metal-Organic Frameworks, pp. 25–52. https://doi.org/10.2307/j.ctvcmxprm.5. Available at:

Mitrović, A., Zdujić, M., 2013. Mechanochemical treatment of Serbian kaolin clay to obtain a highly reactive pozzolana. J. Serb. Chem. Soc. 78 (4), 579–590. https://doi.org/10.2298/JSC120829107M. Available at:

Mohammadi, T., Pak, A., 2002. Making zeolite A membrane from kaolin by electrophoresis. Microporous Mesoporous Mater. 56 (1), 81–88. https://doi.org/10.1016/S1387-1811(02)00444-4. Available at:

Moshoeshoe, M., Silas Nadiye-Tabbiruka, M., Obuseng, V., 2017. A review of the chemistry, structure, properties and applications of zeolites. Am. J. Mater. Sci. 2017 (5), 196–221. https://doi.org/10.5923/j.materials.20170705.12. Available at:

Moumin, G., et al., 2019. Solar treatment of cohesive particles in a directly irradiated rotary kiln. Sol. Energy 182 (January), 480–490. https://doi.org/10.1016/j.solener.2019.01.093. Available at:

Murat, M., et al., 1992. Synthesis of zeolites from thermally activated kaolinite. Some observations on nucleation and growth. Clay Miner. 27 (1), 119–130. https://doi.org/10.1180/claymin.1992.027.1.12. Available at:

Neises, M., et al., 2012. Solar-heated rotary kiln for thermochemical energy storage. Sol. Energy 86 (10), 3040–3048. https://doi.org/10.1016/j.solener.2012.07.012. Available at:

Novembre, D., et al., 2011. Synthesis and characterization of Na-X, Na-A and Na-P zeolites and hydroxysodalite from metakaolinite. Clay Miner. 46 (3), 339–354. https://doi.org/10.1180/claymin.2011.046.3.339. Available at:

Okada, K.O.N., 1986. Characterization of spinel phase formed in the kaolin-mullite thermal sequence. Commun. Am. Ceram. Soc. 69 (10), C-251–C-253. https://doi.org/10.1111/j.1151-2916.1987.tb05749.x. Available at:

Okada, K., Otsuka, N., 1986. Characterization of the spinel phase from SiO2-Al2O3 xerogels and the formation process of mullite. J. Am. Ceram. Soc. 69 (9), 652–656. https://doi.org/10.1111/j.1151-2916.1986.tb07466.x. Available at:

Oleksiak, M.D., et al., 2016. Nucleation of FAU and LTA zeolites from heterogeneous aluminosilicate precursors. Chem. Mater. 28 (14), 4906–4916. https://doi.org/10.1021/acs.chemmater.6b01000. Available at:

Percival, H.J., Duncan, J.F., Foster, P.K., 1974. Interpretation of the kaolinite-mullite reaction sequence from. J. Am. Ceram. Soc. 57 (February), 57–61.

Ptáček, P., et al., 2010. The kinetics of Al-Si spinel phase crystallization from calcined kaolin. J. Solid State Chem. 183 (11), 2565–2569. https://doi.org/10.1016/j.jssc.2010.08.030. Available at:

Ptáček, P., et al., 2011. Mid-infrared spectroscopic study of crystallization of cubic spinel phase from metakaolin. J. Solid State Chem. 184 (10), 2661–2667. https://doi.org/10.1016/j.jssc.2011.07.038. Available at:

Renewable Energy Sources and Climate Change Mitigation: Special Report of the Intergovernmental Panel on Climate Change, 2011. Cambridge: Cambridge University Press. https://doi.org/10.1017/CBO9781139151153. Available at:
Saikia, N.J., et al., 2003. Characterization, beneficiation and utilization of a kaolinite clay from Assam, India. Appl. Clay Sci. 24 (1–2), 93–103. https://doi.org/10.1016/S0169-1317(03)00151-0. Available at:
Salih, A., Williams, C., Khanaqa, P., 2020. Synthesis of zeolite A from Iraqi natural kaolin using a conventional hydrothermal synthesis technique. UKH J Sci. Eng. 4 (2), 11–23. https://doi.org/10.25079/ukhjse.v4n2y2020.pp11-23. Available at:
Sazali, N., Harun, Z., 2022. One shot of the hydrothermal route for the synthesis of zeolite LTA using kaolin. J. Inorg. Organomet. Polym. Mater. 32 (9), 3508–3520. https://doi.org/10.1007/s10904-022-02369-y. Available at:
Schwanke, A.J., et al., 2022. Sustainable conversion of Brazilian Amazon kaolin mining waste to zinc-based Linde Type A zeolites with antibacterial activity. J. Clean. Prod. 338 (December 2021) https://doi.org/10.1016/j.jclepro.2022.130659. Available at:
Sharma, P., et al., 2012. NaA zeolite cubic crystal formation and deformation: cubes with crystalline core, simultaneous growth of surface and core crystals, and layer-by-layer destruction. RSC Adv. 2 (20), 7809–7823. https://doi.org/10.1039/c2ra20567j. Available at:
Soares, R. de M., et al., 2007. Structural characterization of mullites synthesized by thermal decomposition of topaz. Mater. Res. 10 (1), 75–78. https://doi.org/10.1590/S1516-14392007000100016. Available at:
Sonuparlak, B., Sarikaya, M., Aksay, I.A., 1987. Spinel phase formation during the 980°C exothermic reaction in the kaolinite-to-mullite reaction series. J. Am. Ceram. Soc. 70 (11), 837–842. https://doi.org/10.1111/j.1151-2916.1987.tb05637.x. Available at:
Sperinck, S., et al., 2011. Dehydroxylation of kaolinite to metakaolin - a molecular dynamics study. J. Mater. Chem. 21 (7), 2118–2125. https://doi.org/10.1039/c0jm01748e. Available at:
Tasiopoulou, T., et al., 2023. Production-process simulation and life-cycle assessment of metakaolin as supplementary cementitious material. Eng. 4 (1), 761–779. https://doi.org/10.3390/eng4010046. Available at:
Teklay, A., et al., 2014. Calcination of kaolinite clay particles for cement production: a modeling study. Cement Concr. Res. 61–62, 11–19. https://doi.org/10.1016/j.cemconres.2014.04.002. Available at:
Urbonavicius, M., et al., 2020. Production of gamma alumina using plasma-treated aluminum and water reaction byproducts. Materials 13 (6), 1–12. https://doi.org/10.3390/ma13061300. Available at:
Zhou, C., et al., 2013. Characteristics and evaluation of synthetic 13X zeolite from Yunnan's natural halloysite. J. Porous Mater. 20 (4), 587–594. https://doi.org/10.1007/s10934-012-9631-9. Available at:
Zhou, H.M., Qiao, X.C., Yu, J.G., 2013. Influences of quartz and muscovite on the formation of mullite from kaolinite. Appl. Clay Sci. 80 (81), 176–181. https://doi.org/10.1016/j.clay.2013.04.004. Available at: